# Synergistically coupling CoS/FeS₂ heterojunction nanosheets on MXene via dual molten salts etching strategy for efficient oxygen evolution reaction

Zuliang Zhang,[a,1] Tian Liang,[b,1] Chulong Jin,[a] Shuyi Zhang,[d] Yuanyuan Cui,[c,*] Jinxing Chen,[d,*] Xiaojun Zeng[a,*]


[a] National Engineering Research Center for Domestic & Building Ceramics, School of Materials Science and Engineering, Jingdezhen Ceramic University, Jingdezhen 333403, China

[b] Hubei Key Laboratory of Radiation Chemistry and Functional Materials, School of Nuclear Technology and Chemistry & Biology, Hubei University of Science and Technology, Xianning 437100, China

[c] School of Materials Science and Engineering, Shanghai University, Shanghai 200444, China

[d] Institute of Functional Nano & Soft Materials (FUNSOM), Joint International Research Laboratory of Carbon-Based Functional Materials and Devices, Jiangsu Key Laboratory for Carbon-Based Functional Materials & Devices, Soochow University, Suzhou 215123, China


* Corresponding authors, E-mail: zengxiaojun@jcu.edu.cn (X.J. Zeng), cui-yy@shu.edu.cn (Y.Y. Cui), chenjinxing@suda.edu.cn (J.X. Chen)

[1] These authors contributed equally to this work.

## 1. Characterization

The morphology and microstructure of the samples were examined using the field emission scanning electron microscopy (SEM, JSM-6700F, JEOL, Japan) and transmission electron microscopy (TEM, JEM-2100F, JEOL). The crystallographic information of the samples was collected by an X-ray diffractometer (XRD, D8-Advance, Bruker, Germany). Detailed elemental composition and chemical states of the samples were determined using X-ray photoelectron spectroscopy (XPS, Thermo escalab 250Xi). Elemental content was analyzed through inductively coupled plasma optical emission spectroscopy (ICP-OES, Avio 500, PerkinElmer, USA). The BET surface area and pore size of the samples were analyzed using $N_2$ adsorption-desorption isotherms on the Quantachrome NovaWin Surface Area Analyzer (Quantachrome Nova 2000e, USA).

## 2. Electrocatalytic measurements

The electrochemical performance of the samples was evaluated using a three-electrode system. The counter electrode was a platinum wire, while the reference electrode was Hg/HgO and the electrolyte was KOH solution (1 M). Electrochemical experiments were conducted using a CHI760E electrochemical workstation connected to a rotating disk electrode (RRDE-3A, ALS Inc., Tokyo, Japan). The catalyst ink was formulated at a ratio of 4 mg sample to 1 mL of 5 wt% Nafion solution. After being ultrasonically dispersed for 6 h, the catalyst ink was drop-cast onto the surface of a polished glassy carbon electrode (diameter of 3 mm) at a loading amount of 0.2 mg $cm^{-2}$. The ink-coated electrode was air-dried thoroughly at room temperature. The OER performance of the samples was investigated using cyclic voltammetry (CV), linear sweep voltammetry (LSV), and electrochemical impedance spectroscopy (EIS) in a three-electrode configuration. CV curves were recorded with a scan rate of 20~100 mV $s^{-1}$. The double-layer capacitance ($C_{dl}$) was determined from the CV curves in the non-Faradaic region (0.9~1.0 V $vs.$ RHE). LSV curves were tested at a scan rate
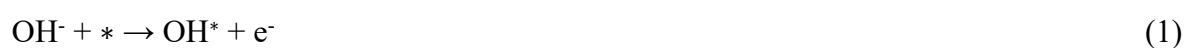
of 5 mV s$^{-1}$. The chronoamperometry technique was employed to measure the current at a constant potential of 1.52 V (*vs.* RHE). EIS measurements were conducted over a frequency range of 0.01 Hz to 100 kHz with an AC voltage amplitude of 5 mV. All electrochemical potentials were converted to the reversible hydrogen electrode (RHE) scale according to the Nernst equation: $E_{RHE} = E_{Hg/HgO} + 0.0591 \times pH + 0.098$. The overpotential is defined as the potential difference between $E_{RHE}$ and $E_0$ (OER equilibrium potential, 1.23 V). The overpotential mentioned in the main text has been iR-corrected.

### 3. Density functional theory (DFT) calculations

All calculations were conducted within the framework of density functional theory (DFT), utilizing the Vienna Ab initio Simulation Package (VASP) for the evaluation of Gibbs free energy and density of states (DOS) [1]. The exchange-correlation energy was computed using the generalized gradient approximation (GGA) and the Perdew-Burke-Ernzerhof (PBE) functional [2]. The plane-wave cutoff energy was set to 400 eV. For determining the optimized geometric structures, the convergence criterion for atomic forces was set to 0.001 eV/Å$^{-1}$. Additionally, to prevent interactions between different slabs, a sufficient vacuum space of 15 Å was included in the construction of the surface slab model. A single gamma-point grid was used for sampling the Brillouin zone during geometric optimization. The DFT-D3 dispersion correction method was used to illustrate the weak interaction betweenthe slab and the active species [3].

### 4. Theoretical model

The OER cycle proposed by precious work [4-8]. In detail, For OER in alkaline electrolyte (pH=14), since OH$^-$ may act as an electron donor, the overall reaction scheme of OER can be expressed as:

$$OH^- + * \rightarrow OH^* + e^- \tag{1}$$

$$OH^* + OH^- \rightarrow O^* + H_2O \text{ (l)} + e^- \tag{2}$$

$$O^* + OH^- \rightarrow OOH^* + e^- \tag{3}$$

$$OOH^* + OH^- \rightarrow O_2(g) + H_2O(l) + e^- + * \tag{4}$$

For each elementary step associated with OER, the Gibbs reaction free energy $\Delta G$ is defined as the difference between free energies of the initial and final states, given by the following expression:
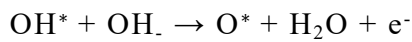
$$\Delta G = \Delta E + \Delta ZPE - T\Delta S \tag{5}$$

where $\Delta E$ is the reaction energy of reactant and product molecules adsorbed on catalyst surface, and $\Delta ZPE$ and $\Delta S$ are the change in zero-point energies and entropy in the reaction.

The reaction free energy of (1)-(4) for the OER can be determined from the following equations:

$$OH^- + * \rightarrow OH^* + e^-$$
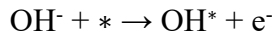
$$\Delta G_1 = G_{OH^*} + G_{e^-} - G_{OH^-} - G^*$$

$$= G_{OH^*} + G_{e^-} - (G_{H2O}(l) + G_{e^-} - 1/2G_{H2}(g)) - G^*$$

$$= G_{OH^*} + 1/2G_{H2}(g) - G_{H2O}(l) - G^*$$

$$= \Delta G_{OH^*} \tag{6}$$

$$OH^* + OH_- \rightarrow O^* + H_2O + e^-$$

$$\Delta G_2 = G_{O^*} + G_{H2O} + G_{e^-} - G_{OH^-} - G_{OH^*}$$

$$= G_{O^*} + G_{H2O} + G_{e^-} - [GH2O(l) + Ge^- - 1/2G_{H2}(g)] - G_{OH^*}$$

$$= (G_{O^*} + G_{H2} - G_{H2O}(l) - G^*) - (G_{OH^*} + 1/2G_{H2}(g) - G_{H2O}(l) - G^*)$$

$$= \Delta G_{O^*} - \Delta G_{OH^*} \tag{7}$$

$$O^* + OH^- \rightarrow OOH^* + e^-$$
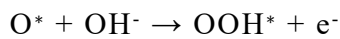
$$\Delta G_3 = G_{OOH^*} + G_{e^-} - G_{O^*} - G_{OH^-}$$

$$= G_{OOH^*} + G_{e^-} - G_{O^*} - (G_{H2O}(l) + G_{e^-}1/2G_{H2}(g))$$

$$= (G_{OOH*} + 3/2G_{H2}(g) - 2G_{H2O}(l) - G_*) - (G_{O*} + G_{H2}(g) - G_{H2O}(l) - G_*)$$

$$= \Delta G_{OOH*} - \Delta G_{O*} \tag{8}$$

$$OOH^* + OH^- \rightarrow O_2(g) + H_2O(l) + e^- + *$$
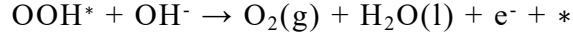
$$\Delta G_4 = G_{O2}(g) + G_{H2O}(l) + G_{e^-} + * - G_{OOH*} - G_{OH^-} = (2G_{H2O}(l) - 2G_{H2}(g) + 4 \times 1.23)$$

$$+ G_{H2O}(l) + G_{e^-} + * - G_{OOH*} - (G_{H2O}(l) + G_{e^-} - 1/2G_{H2}(g))$$

$$= 2G_{H2O}(l) - 1/2G_{H2}(g) + * - G_{OOH*}$$

$$= 4.92 - \Delta G_{OOH*} \tag{9}$$

With this method, the theoretical overpotential ($U^{OER}$) at standard condition is defined as:

$$U^{OER} = (G^{OER} / e) - 1.23 \tag{10}$$

where $G^{OER}$ is the potential determining step defined as the highest free-energy step in the OER, and e is unit charge.
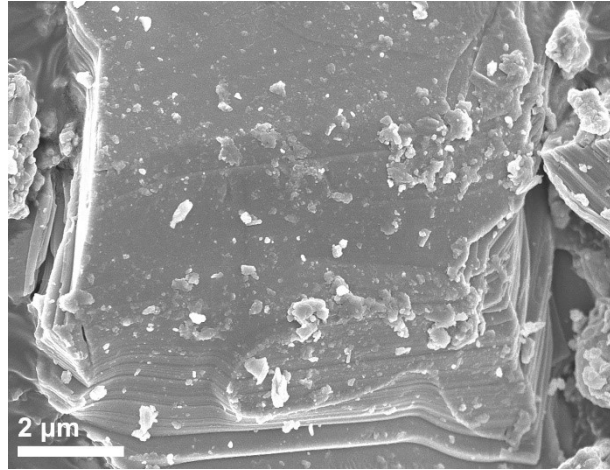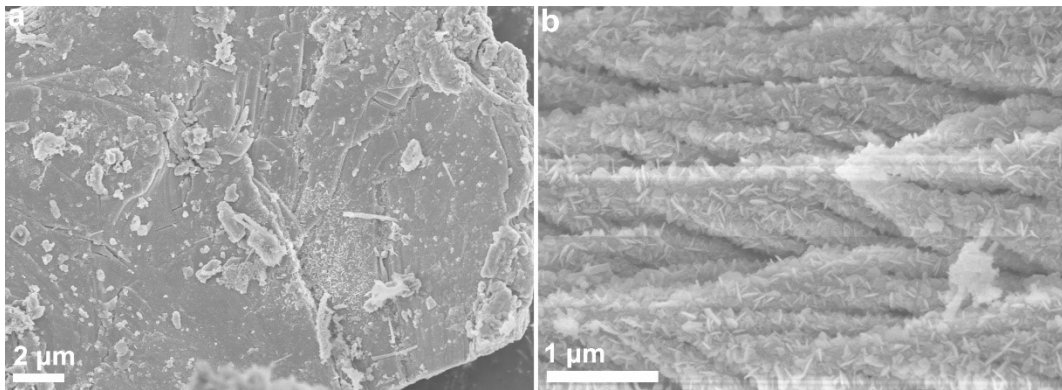
**Figure S1.** SEM images of Ti$_3$AlC$_2$ MAX.



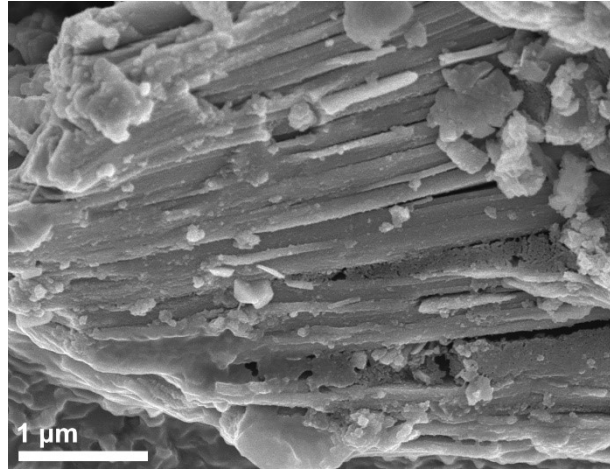**Figure S2.** SEM images of MAX@NaCl/KCl.

**Figure S3.** SEM images of cross-section for MAX@NaCl/KCl-S.
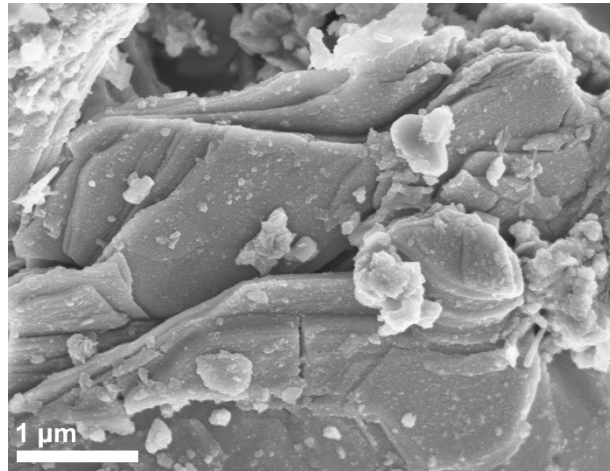


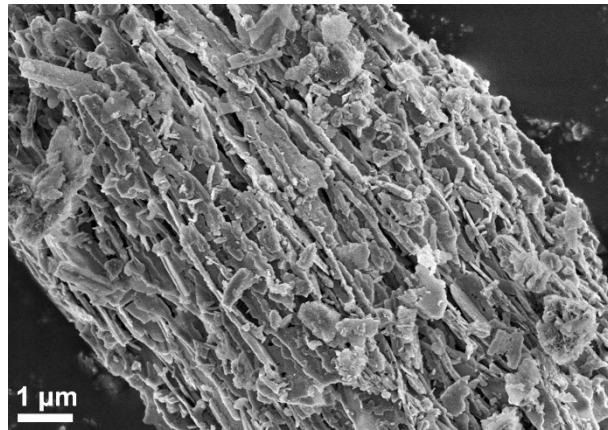**Figure S4.** SEM images of longitudinal direction for MAX@NaCl/KCl-S.

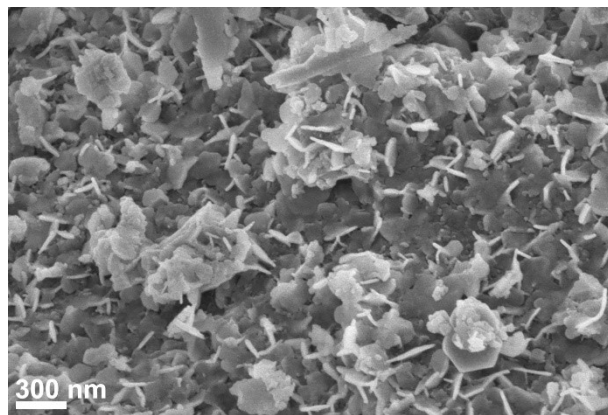**Figure S5.** SEM images of cross-section for MXene@Co$_{0.7}$Fe$_{0.3}$.



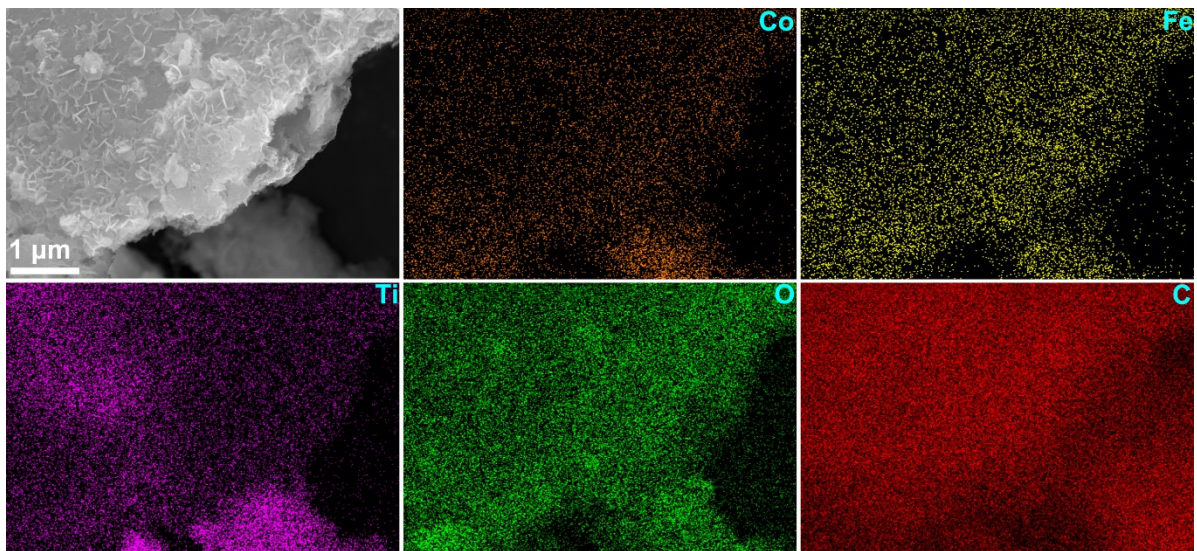**Figure S6.** SEM images of longitudinal direction for MXene@Co$_{0.7}$Fe$_{0.3}$.

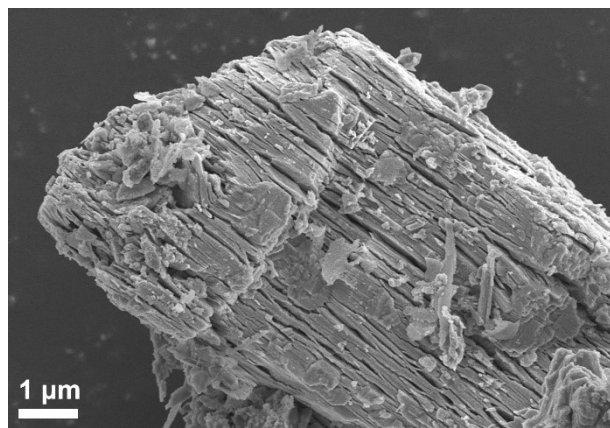**Figure S7.** Elemental mapping images of MXene@$Co_{0.7}Fe_{0.3}$.



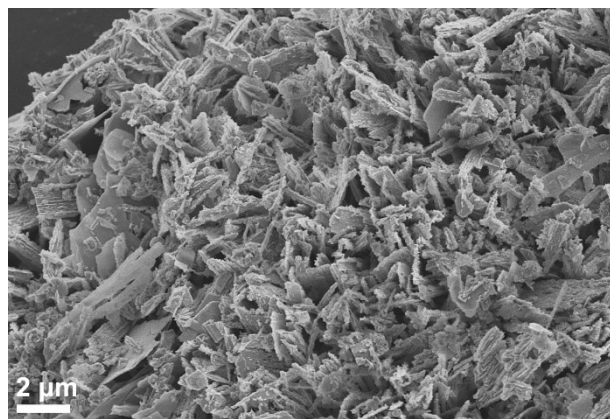**Figure S8.** SEM images of cross-section for MXene@$CoS/FeS_2$.

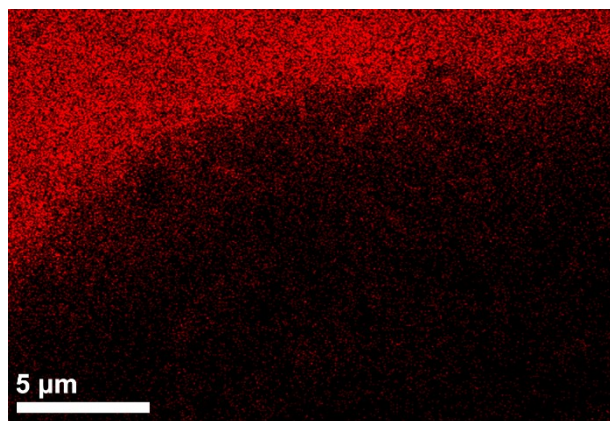**Figure S9.** SEM images of longitudinal direction for MXene@CoS/FeS$_2$.



**Figure S10.** Elemental mapping images of C elements for MXene@CoS/FeS$_2$.
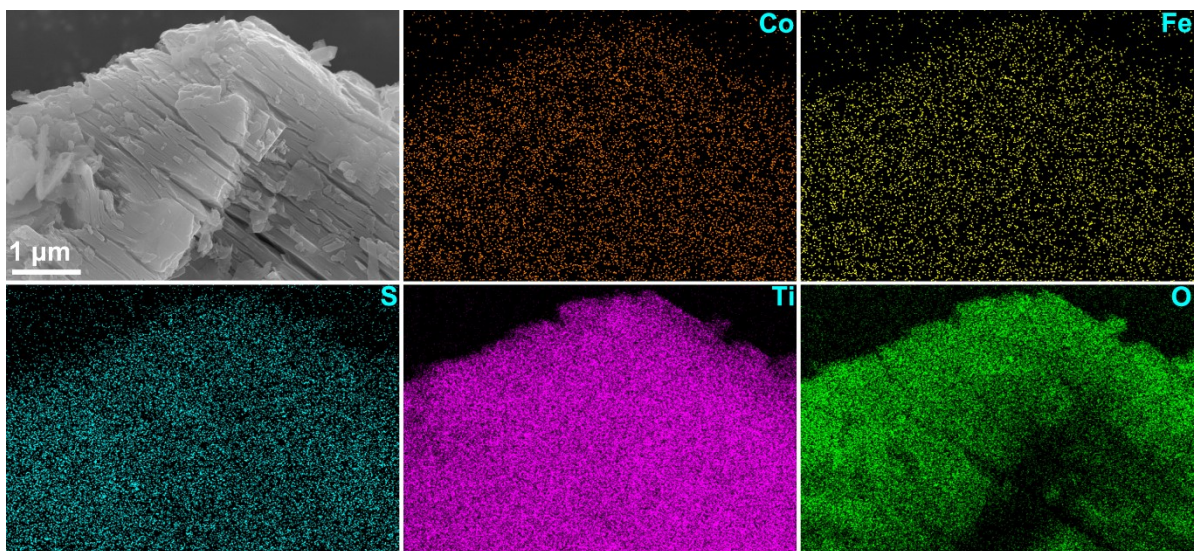
**Figure S11.** Elemental mapping images of MXene@CoS/FeS$_2$.
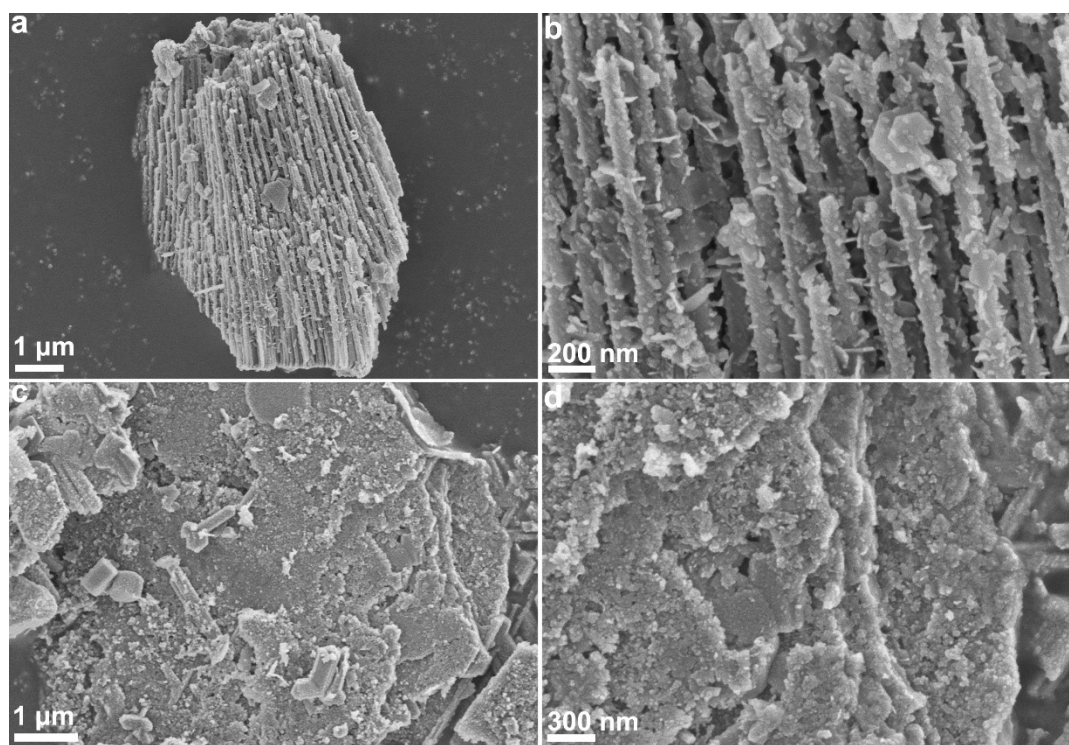


**Figure S12.** SEM images of MXene@CoS.
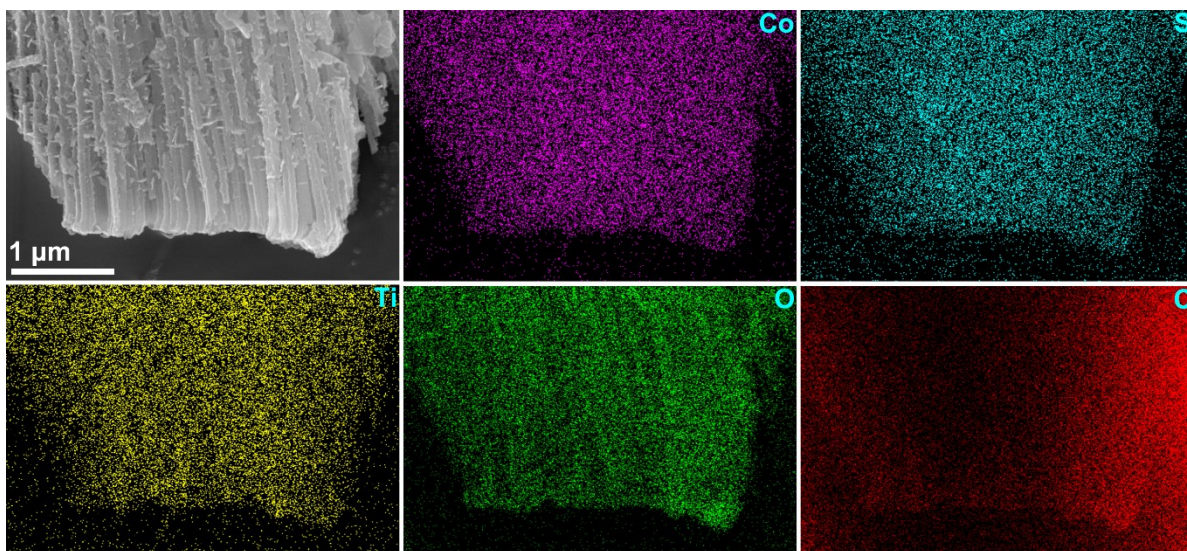
**Figure S13.** Elemental mapping images of MXene@CoS.
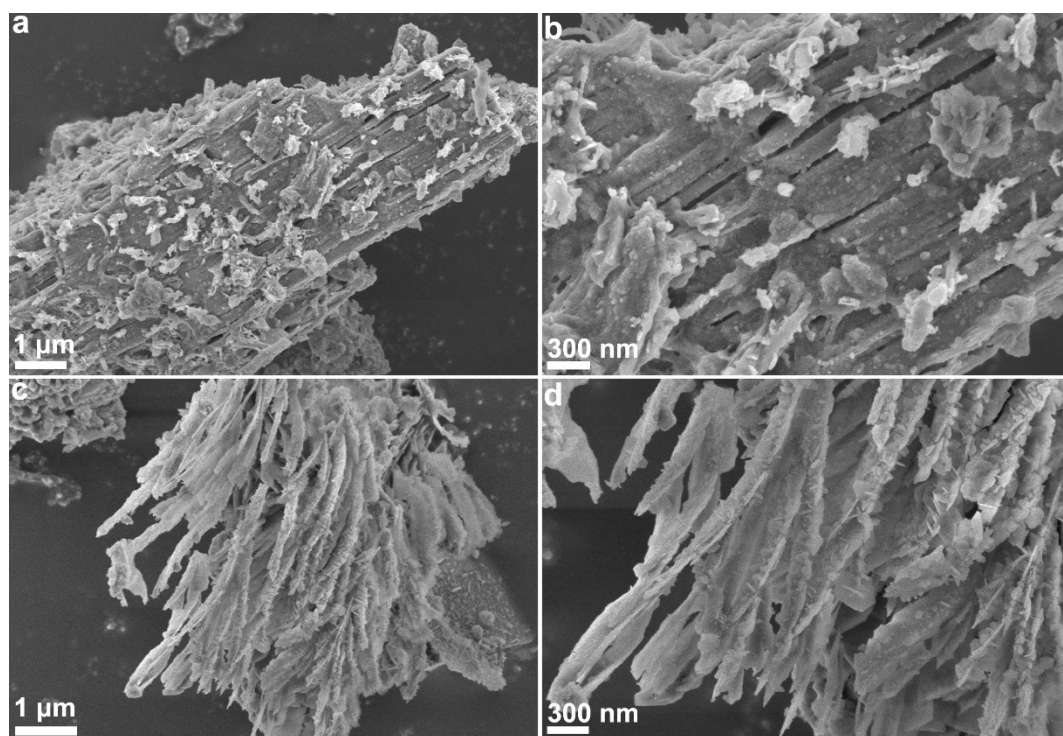


**Figure S14.** SEM images of MXene@FeS$_2$.
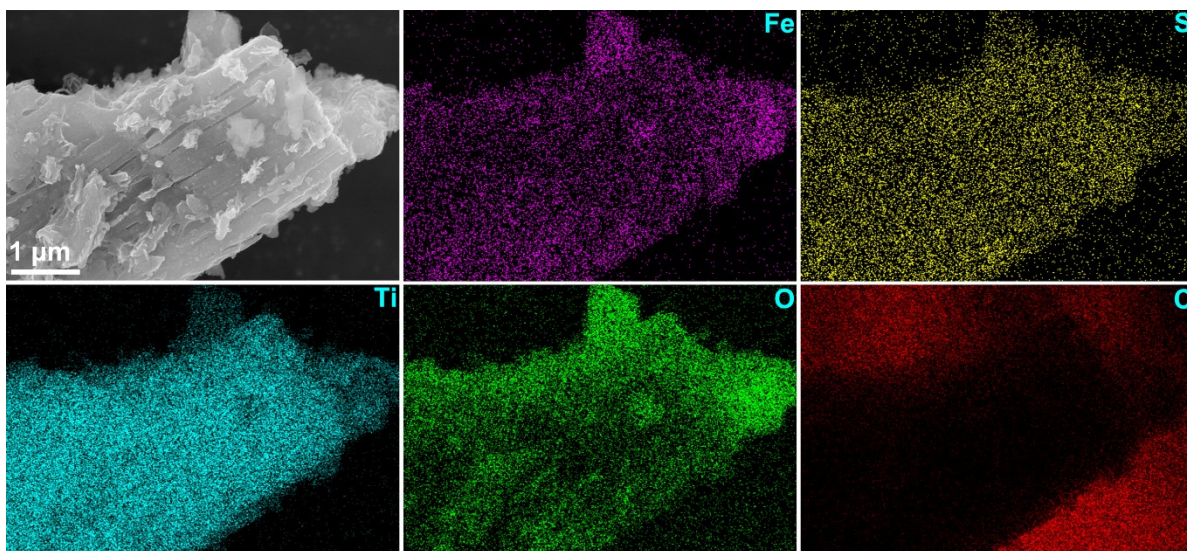
**Figure S15.** Elemental mapping images of MXene@FeS$_2$.
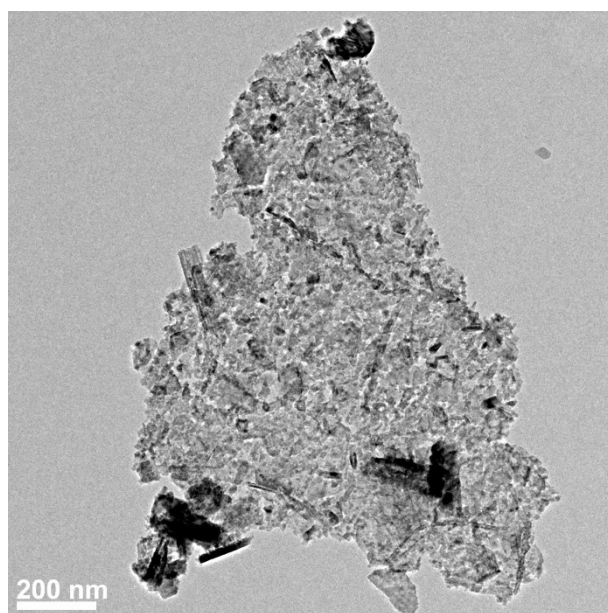


**Figure S16.** TEM images of MAX@NaCl/KCl-S.
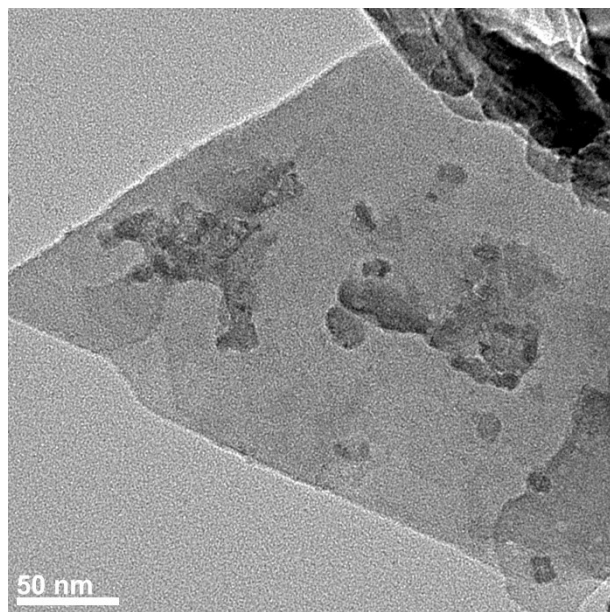
**Figure S17.** TEM images of surface for MXene@CoS/FeS$_2$.
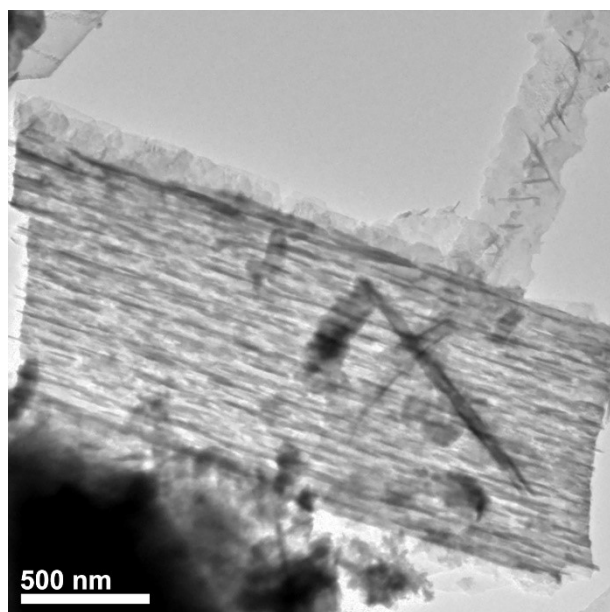


**Figure S18.** TEM images of cross-section for MXene@CoS/FeS$_2$.
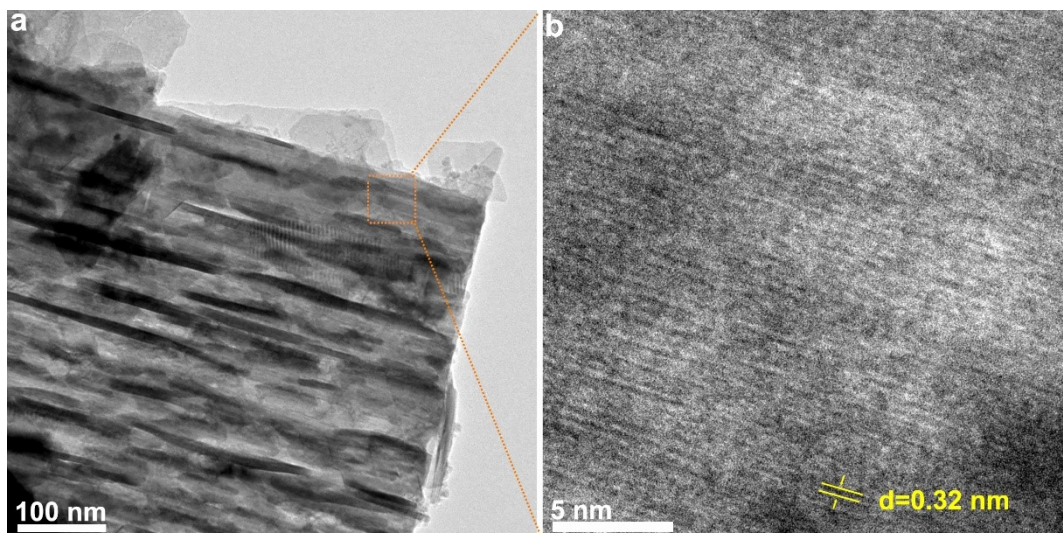
**Figure S19.** (a) TEM and (b) images of MXene@CoS/FeS$_2$.
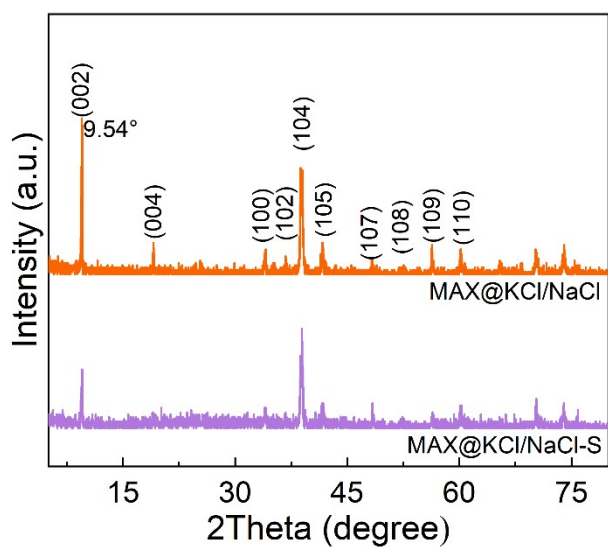


**Figure S20.** XRD patterns of MAX@NaCl/KCl and MAX@NaCl/KCl-S.
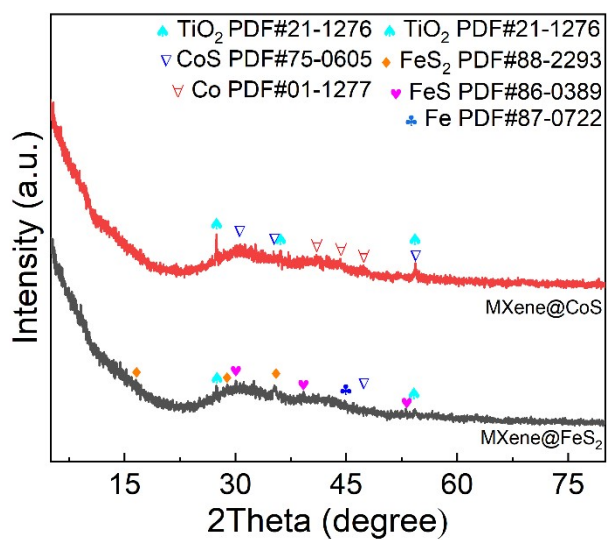
**Figure S21.** XRD patterns of MXene@CoS and MXene@FeS$_2$.
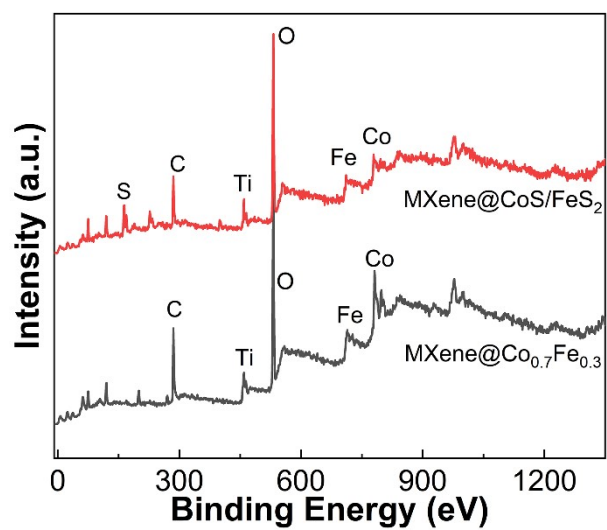


**Figure S22.** XPS survey spectra of MXene@Co$_{0.7}$Fe$_{0.3}$ and MXene@CoS/FeS$_2$.
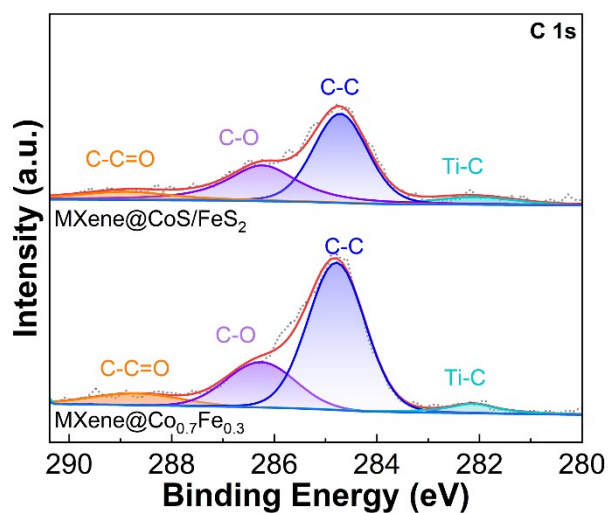
**Figure S23.** High-resolution XPS spectra of C 1s for MXene@$Co_{0.7}Fe_{0.3}$ and MXene@$CoS/FeS_2$.
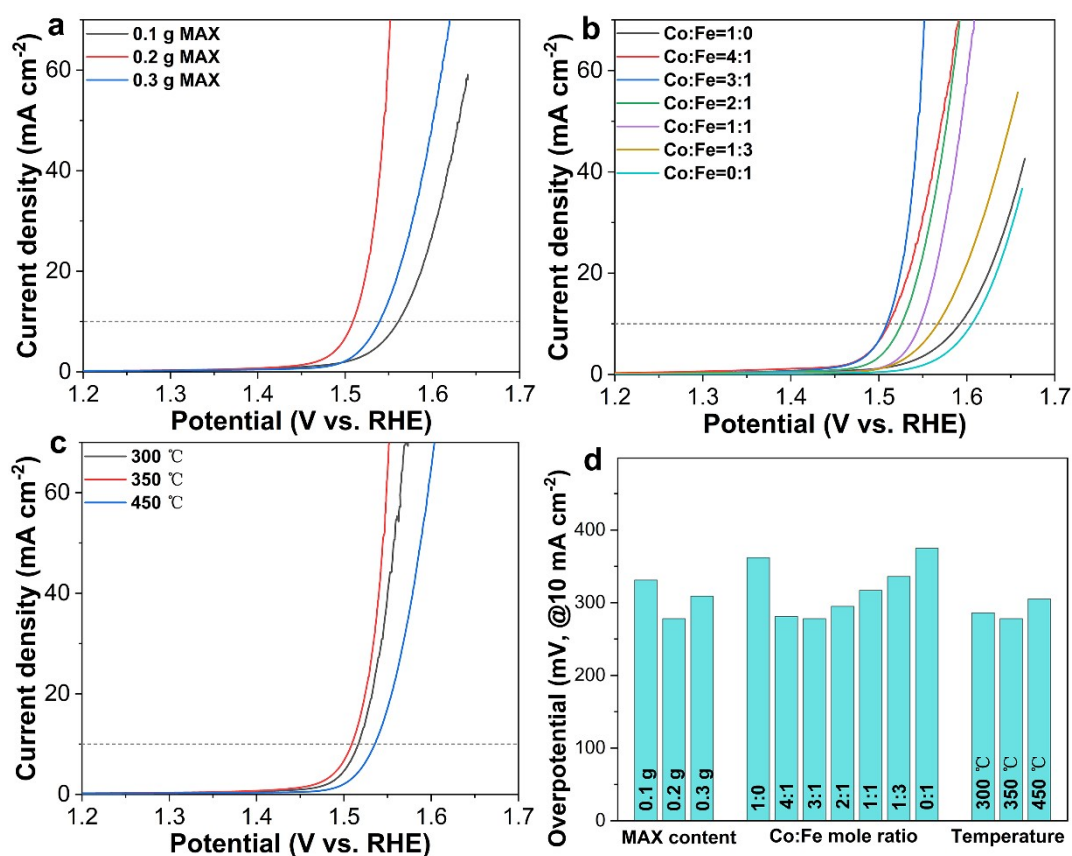


**Figure S24.** LSV polarization curves for MXene@$CoS/FeS_2$ obtained under various conditions: (a) MAX content, (b) mole ratios of Co salt and Fe salt, and (c) sulfidation temperatures. (d) Overpotentials of all the catalysts at the current densities of 10 mA $cm^{-2}$.
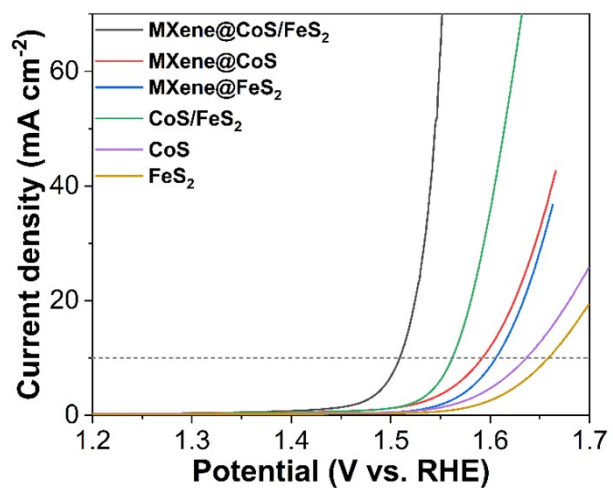
**Figure S25.** LSV curves of CoS, $FeS_2$, $CoS/FeS_2$, MXene/CoS, MXene/$FeS_2$, and MXene@CoS/$FeS_2$.
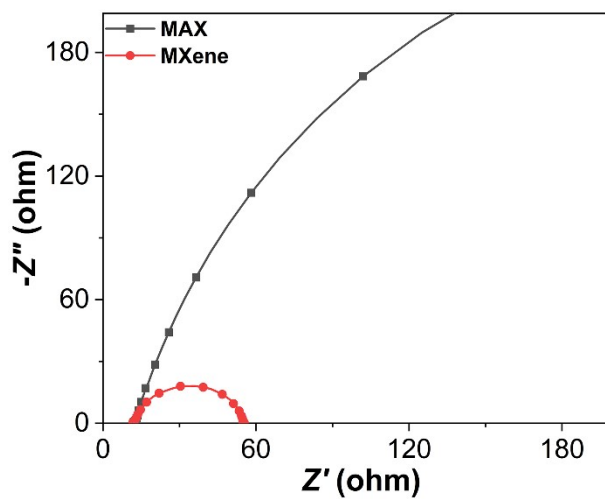


**Figure S26.** Nyquist plots for MXene and MAX.
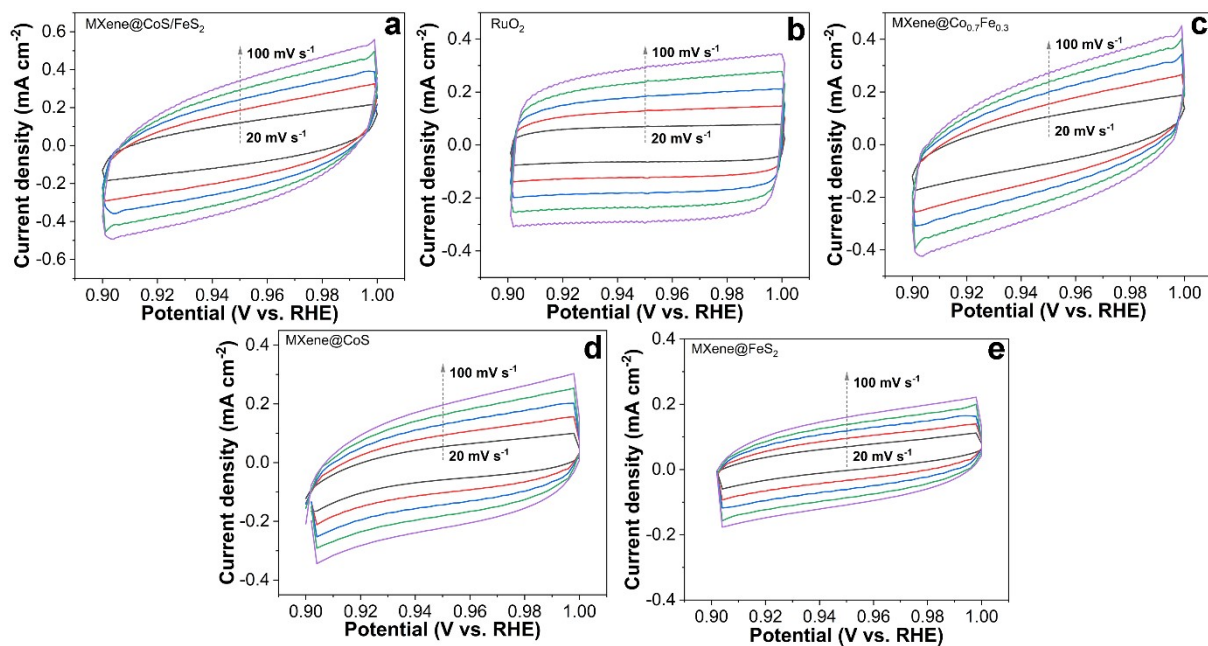
**Figure S27.** CV curves of (a) MXene@CoS/FeS$_2$, (b) RuO$_2$, (c) MXene@Co$_{0.7}$Fe$_{0.3}$, (d) MXene@CoS, and (e) MXene@FeS$_2$ catalysts at the scan rates of 20, 40, 60, 80, and 100 mV s$^{-1}$.
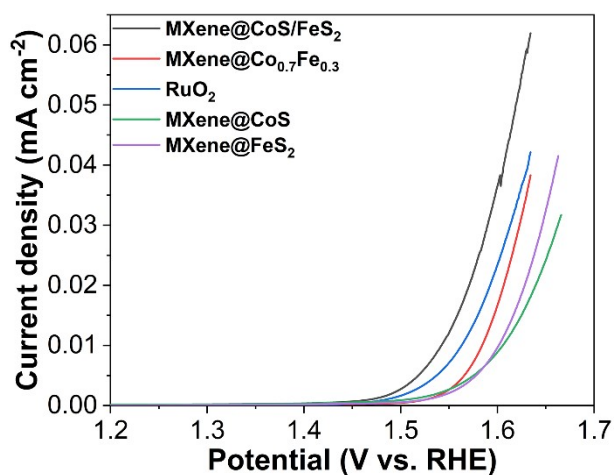


**Figure S28.** LSV polarization curves normalized by ECSA.
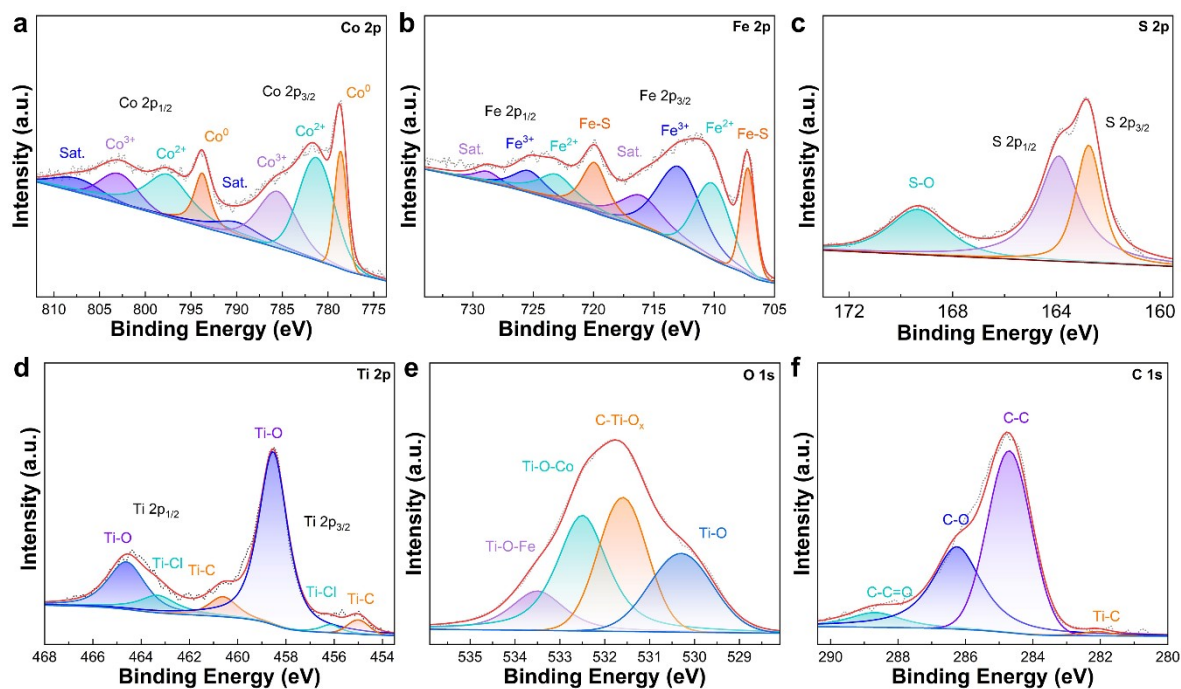
**Figure S29.** High-resolution XPS spectra of (a) Co 2p, (b) Fe 2p, (c) S 2p, (d) Ti 2p, (e) O 1s, and (f) C 1s for MXene@CoS/FeS$_2$ catalyst after long-term stability test.
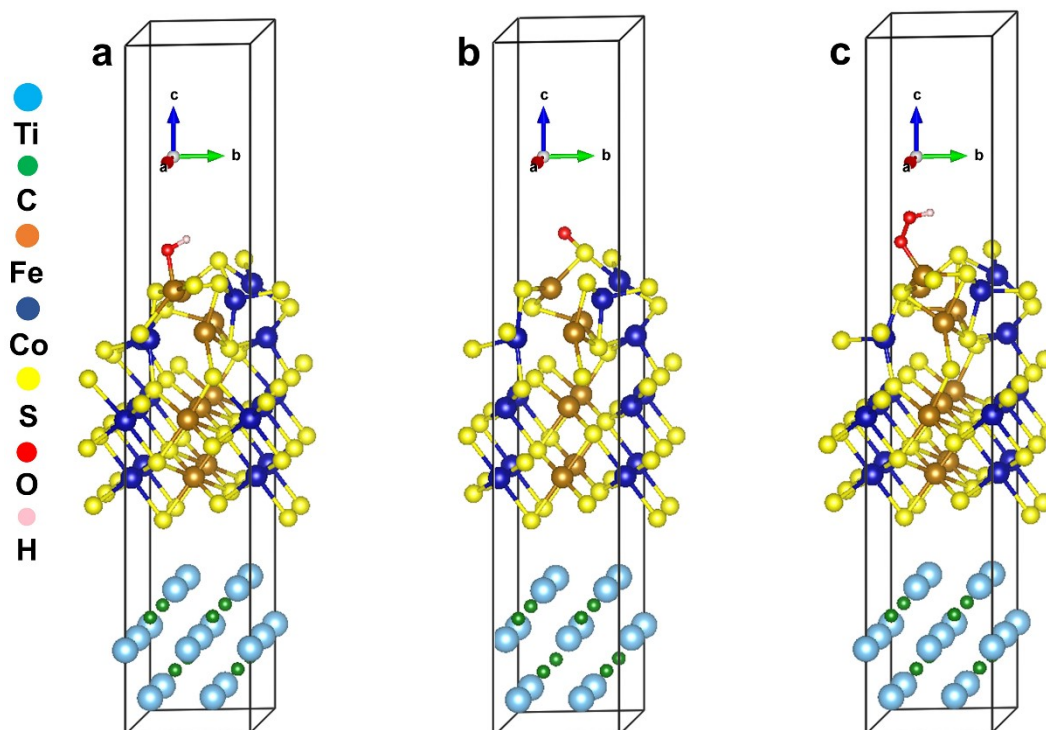


**Figure S30.** Schematic diagram of MXene@CoS/FeS$_2$ adsorption models for (a) *OH, (b) *O, and (c) *OOH.
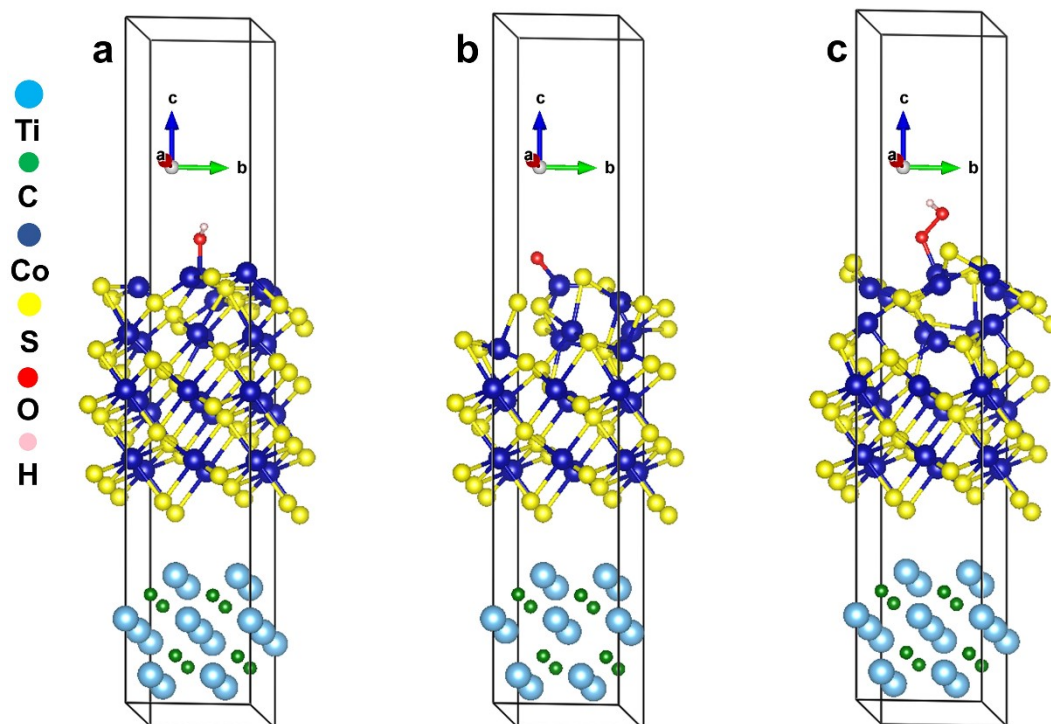
**Figure S31.** Schematic diagram of MXene@CoS adsorption models for (a) *OH, (b) *O, and (c) *OOH.
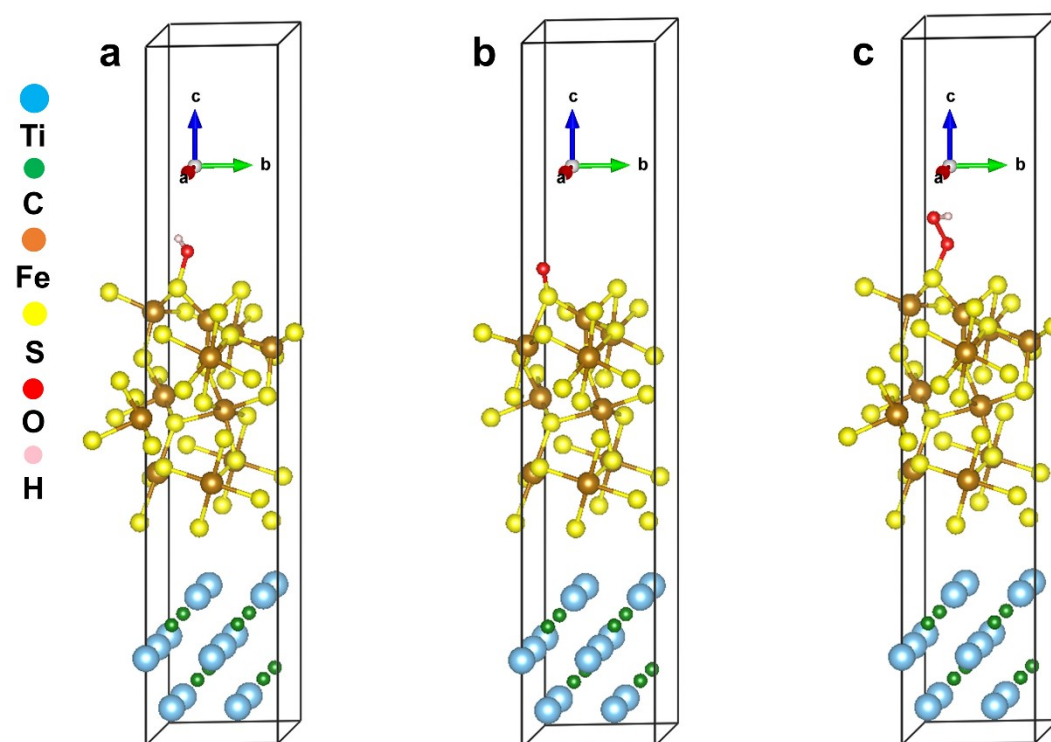


**Figure S32.** Schematic diagram of MXene@FeS$_2$ adsorption models for (a) *OH, (b) *O, and (c) *OOH.
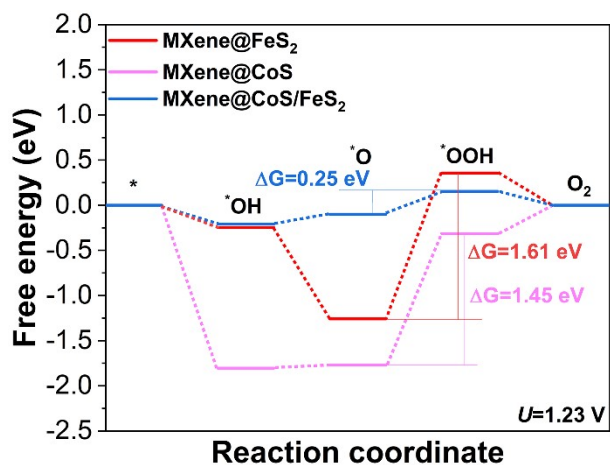
**Figure S33.** Calculated OER free-energy diagrams of catalysts at potential of 1.23 V.
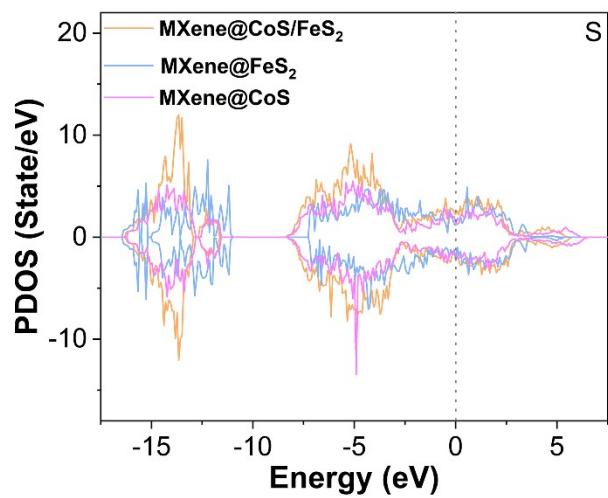


**Figure S34.** PDOS curves of MXene@CoS/FeS$_2$, MXene@CoS and MXene@FeS$_2$.

**Table S1.** Element contents in the MXene@CoS/FeS$_2$ heterostructures detected by XPS technique.

| Elements | Atomic % |
|----------|----------|
| C | 25.14 |
| S | 11.64 |
| O | 46.24 |
| N | 5.05 |
| Ti | 3.66 |
| Co | 4.53 |
| Fe | 3.74 |

**Table S2.** Element contents in the MXene@CoS/FeS$_2$ heterostructures detected by ICP-OES technique.

| Samples | Elements (mass %) | | | |
|---------|------|------|------|------|
| | Co | Fe | Ti | S |
| MXene@CoS | 24.07 | | 15.18 | 7.56 |
| MXene@FeS$_2$ | | 22.90 | 16.86 | 4.23 |
| MXene@CoS/FeS$_2$ | 19.61 | 6.32 | 11.40 | 9.99% |

**Table S3.** Electrocatalytic performances of MXene@CoS/FeS$_2$ and recently advanced OER catalysts.

| Electrocatalysts | Loading (mg cm$^{-2}$) | OER $\eta$ (mV) @10 mA cm$^{-2}$ | Electrolyte | Ref. |
|---|---|---|---|---|
| ACTP5@Co,N-800 | 0.30 | 374 | 0.1 M KOH | [9] |
| MXene/ZIF-67 | 0.5 | 366 | 1 M KOH | [10] |
| NiCoS/Ti$_3$C$_2$T$_x$ | 0.21 | 365 | 1 M KOH | [11] |
| NiCo$_2$O$_4$/MXene | - | 360 | 1 M KOH | [12] |
| BP-CN-c | 0.50 | 350 | 1 M KOH | [13] |
| MnSAC | 0.10 | 350 | 0.1 M KOH | [14] |
| NiO@MXene | - | 346 | 1 M KOH | [15] |
| Ni(OH)$_2$/Ni$_3$S$_2$ | - | 340 | 1 M KOH | [16] |
| MoSe$_2$/MXene | 2-3 | 340 | 1 M KOH | [17] |
| Co/CoSe | - | 320 | 1 M KOH | [18] |
| CoFe PBA@CoP/NF | - | 312 | 1 M KOH | [19] |
| CoSe$_2$@MoSe$_2$ | 0.54 | 309 | 1 M KOH | [20] |
| Fe-Co-CN/rGO-700 | 0.25 | 308 | 1 M KOH | [21] |
| CoSA/N,S-HCS | 1.50 | 306 | 1 M KOH | [22] |
| FeS$_2$/TiO$_2$ | 0.25 | 300 | 1 M KOH | [23] |
| Co$_3$O$_4$/CC | - | 300 | 1 M KOH | [24] |
| MXene/NiCoFeP$_x$-NC | 0.20 | 293 | 1 M KOH | [25] |
| P-Co$_3$O$_4$ | 0.30 | 290 | 1 M KOH | [26] |
| Ni/Ni$_2$P@N-CNF | 0.25 | 285 | 1 M KOH | [27] |
| P$_{30}$-doped Fe/NF | - | 284 | 1 M KOH | [28] |
| (CoFeNiMnCu)S$_2$ | 0.16 | 284 | 1 M KOH | [29] |
| MXene@CoS/FeS$_2$ | 0.2 | 278 | 1 M KOH | This work |
| Co-MOF-NK | 1.00 | 268 | 1 M KOH | [30] |
| Pt$_{SA}$-PtCo NCs/N-CNTs | - | 252 | 1 M KOH | [31] |
| Ni$_{0.85}$Se-O/CN | - | 240 | 1 M KOH | [32] |

**Table S4.** $C_{dl}$ and ECSA values of the the samples.

| Samples | $C_{dl}$ (mF cm$^{-2}$) | ECSA |
|---|---|---|
| MXene@CoS/FeS$_2$ | 5.7 | 142.5 |
| MXene@Co$_{0.7}$Fe$_{0.3}$ | 4.5 | 112.5 |
| RuO$_2$ | 5.4 | 135 |
| MXene@CoS | 3.8 | 95 |
| MXene@FeS$_2$ | 2.5 | 62.5 |

Note: ECSA values were calculated using the following equation: ECSA = $C_{dl}/C_s$, where $C_s$ is the specific capacitance (typically 40 μF cm$^{-2}$ in 1 M KOH).

**References**

[1] G. Kresse, J. Hafner, Ab initio molecular dynamics for liquid metals, Phy. Rev. B 1993, 47, 558.

[2] X. J. Zeng, H. Q. Zhang, R. H. Yu, G. D. Stucky and J. S. Qiu, A phase and interface co-engineered MoP$_x$S$_y$@NiFeP$_x$S$_y$@NPS-C hierarchical heterostructure for sustainable oxygen evolution reaction, *J. Mater. Chem. A*, 2023, 11(26), 14272-14283.

[3] G. Kresse, J. Furthmüller, Efficient iterative schemes for ab initio total-energy calculations using a plane-wave basis set, Phy. Rev. B 1996, 54, 11169.

[4] J. Rossmeisl, Z.-W. Qu, H. Zhu, G.-J. Kroes and J. K. Nørskov, Electrolysis of Water on Oxide Surfaces, *J. Electroanal. Chem.*, 2007, 607, 83–89.

[5] J. Rossmeisl, A. Logadottir and J. K. Nørskov, Electrolysis of Water on (Oxidized) Metal Surfaces, *Chem. Phys.*, 2005, 319, 178–184.

[6] I. C. Man, H.-Y. Su, F. Calle-Vallejo, H. A. Hansen, J. I. Martínez, N. G. Inoglu, J. Kitchin, T. F. Jaramillo, J. K. Nørskov and J. Rossmeisl, Universality in Oxygen Evolution Electrocatalysis on Oxide Surfaces, *ChemCatChem*, 2011, 3(7), 1159–1165.

[7] E. Larsson, An X-ray investigation of Ni-P system and crystal structures of NiP and NiP$_2$, *Arkiv for Kemi*, 1965, 23(34), 335-365.

[8] P. Wang, X. Zhang, J. Zhang, S. Wan, S. Guo, G. Lu, J. Yao and X. Huang, Precise tuning in platinum-nickel/nickel sulfide interface nanowires for synergistic hydrogen evolution catalysis, *Nat. Commun.*, 2017, 8(1), 14580.

[9] J. T. Zhang, T. Zhang, J. Ma, Z. Wang, J. H. Liu and X. Z. Gong, ORR and OER of Co-N codoped carbon-based electrocatalysts enhanced by boundary layer oxygen molecules transfer, *Carbon*, 2021, 172, 556-568.

[10] B. Środa, A. G. Dymerska, B. Zielińska and E. Mijowska, Promotion of MXene (Ti$_3$C$_2$T$_x$) as a robust electrocatalyst for oxygen evolution reaction via active sites of ZIF-67-In situ mechanism investigations, *Int. J. Hydrogen Energy*, 2023, 48(49), 18696-18707.

[11] H. Zou, B. He, P. Kuang, J. Yu and K. Fan, Metal-Organic Framework-Derived Nickel-Cobalt Sulfide on Ultrathin Mxene Nanosheets for Electrocatalytic Oxygen Evolution, *ACS Appl. Mater. Interfaces*, 2018, 10, 22311-22319.

[12] A. Vazhayil, L. Vazhayal, S. Ashok C, J. Thomas and N. Thomas, NiCo$_2$O$_4$/MXene hybrid as an efficient bifunctional electrocatalyst for oxygen evolution and reduction reaction, *ChemCatChem*, 2024, 16, e202301250.

[13] X. Wang, R. K. M. Raghupathy, C. J. Querebillo, Z. Q. Liao, D. Q. Li, K. Lin, M. Hantusch, Z. Sofer, B. H. Li, Z. Zschech, I. M. Weidinger, T. D. Kühne, H. Mirhosseini, M. H. Yu and X. L. Feng, Interfacial covalent bonds regulated electron-deficient 2D black phosphorus for electrocatalytic oxygen reactions, *Adv. Mater.*, 2021, 33(20), 2008752.

[14] H. S. Shang, W. M. Sun, R. Sui, J. J. Pei, L. R. Zheng, J. C. Dong, Z. L. Jiang, D. N. Zhou, Z. B. Zhuang, W. X. Chen, J. T. Zhang, D. S. Wang and Y. D. Li, Engineering isolated Mn-N$_2$C$_2$ atomic interface sites for efficient bifunctional oxygen reduction and evolution reaction, *Nano Lett.*, 2020, 20(7), 5443-5450.

[15] U, Naeem, S. A. Zahra, I. Ali,H. Li, A. Mahmood, S. Rizwan, Unleashing the potential of NiO@V$_2$CT$_x$ MXene-derived electrocatalyst for hydrogen and oxygen evolution, *Int. J. Hydrogen Energy*, 2024, 59, 635-644.

[16] X. Q. Du, Z. Yang, Y. Li, Y. Q. Gong and M. Zhao, Controlled synthesis of Ni(OH)$_2$/Ni$_3$S$_2$ hybrid nanosheet arrays as highly active and stable electrocatalysts for water splitting, *J. Mater. Chem. A*, 2018, 6(16), 6938-6946.

[17] N. Li, Y. Zhang, M. Jia, X. Lv, X. Li, R. Li, X. Ding, Y.Z. Zheng and X. Tao, 1T/2H MoSe$_2$-on-MXene heterostructure as bifunctional electrocatalyst for efficient overall water splitting, *Electrochim. Acta*, 2019, 326, 134976.

[18] Y. T. Wu, F. H. Wang, N. W. Ke, B. B. Dong, A. D. Huang, C. T. Tan, L. J. Yin, X. Xu, L. Y. Xian and S. Agathopoulos, Self-supported cobalt/cobalt selenide heterojunction for highly efficient overall water splitting, *J. Alloy. Compd.*, 2022, 925, 166683.

[19] L. Quan, S. H. Li, Z. P. Zhao, J. Q. Liu, Y. Ran, J. Y. Cui, W. Lin, X. L. Yu, L. Wang, Y. H. Zhang and J. H. Ye, Hierarchically assembling CoFe prussian blue analogue nanocubes on CoP nanosheets as highly efficient electrocatalysts for overall water splitting, *Small Methods* 2021, 5(7), 2100125.

[20] Z. W. Chen, W. W. Wang, S. S. Huang, P. Nina, Y. Wu, C. Y. Gao, T. T. Le, J. T. Zai, Y. Jiang, Z. J. Hu and X. F. Qian, Well-defined CoSe$_2$@MoSe$_2$ hollow heterostructured nanocubes with enhanced dissociation kinetics for overall water splitting, *Nanoscale*, 2020, 12(1), 326-335.

[21] W. H. Fang, J. Wang, Y. Hu, X. Q. Cui, R. F. Zhu, Y. H. Zhang, C. C. Yue, J. Q. Dang, W. Cui, H. Zhao and Z. X. Li, Metal-organic framework derived Fe-Co-CN/reduced graphene oxide for efficient HER and OER, *Electrochim. Acta*, 2021, 365, 137384.

[22] Z. Y. Zhang, X. X. Zhao, S. B. Xi, L. L. Zhang, Z. X. Chen, Z. P. Zeng, M. Huang, H. B. Yang, B. Liu, S. J. Pennycook and P. Chen, Atomically dispersed cobalt trifunctional

electrocatalysts with tailored coordination environment for flexible rechargeable Zn-air battery and self-driven water splitting, *Adv. Energy Mater.*, 2020, 10(48), 2002896.

[23] Z. J. Chen, R. J. Zheng, S. M. Deng, W. F. Wei, W. Wei, B. Ni and H. Chen, Modular design of an efficient heterostructured $FeS_2/TiO_2$ oxygen evolution electrocatalyst via sulfidation of natural ilmenites, *J. Mater. Chem. A*, 2021, 9(44), 25032-25041.

[24] A. B. Urgunde, V. Kamboj, H. P. Kannattil and R. Gupta, Layer-by-Layer Coating of Cobalt-Based Ink for Large-Scale Fabrication of OER Electrocatalyst, *Energy Technol.*, 2019, 7(9), 1900603.

[25] X. J. Zeng, Y. Y. Ye, Y. Q. Wang, R. H. Yu and M. Moskovits, Honeycomb-like $MXene/NiFeP_x$-NC with "continuous" single-crystal enabling high activity and robust durability in electrocatalytic oxygen evolution reactions, *J. Adv. Ceram.*, 2023, 12(3), 553-564.

[26] Y. Lu, C. J. Li, Y. Zhang, X. Cao, G. Xie, M. L. Wang, D. D. Peng, K. Huang, B. W. Zhang, T. Wang, J. S. Wu and Y. Z. Huang, Engineering of cation and anion vacancies in $Co_3O_4$ thin nanosheets by laser irradiation for more advancement of oxygen evolution reaction, *Nano Energy*, 2021, 83, 105800.

[27] X. G. Li, J. H. Zhou, C. Liu, L. Xu, C. L. Lu, J. Yang, H. Pang and W. H. Hou, Encapsulation of Janus-structured $Ni/Ni_2P$ nanoparticles within hierarchical wrinkled N-doped carbon nanofibers: Interface engineering induces high-efficiency water oxidation, *Appl. Catal. B*, 2021, 298, 120578.

[28] Y. Ju, S. Y. Feng, X. B. Wang, M. Li, L. Wang, R. D. Xu and J. L. Wang, Facile Preparation of a Porous Nanosheet $P_X$-Doped Fe Bi-Functional Catalyst with Excellent OER and HER Electrocatalytic Activity, *ChemistrySelect*, 2021, 6, 4979-4990.

[29] M. Moradi, F. Hasanvandian, A. Bahadoran, A. Shokri, S. Zerangnasrabad and B, Kakavandi, New high-entropy transition-metal sulfide nanoparticles for electrochemical oxygen evolution reaction, *Electrochim. Acta*, 2022, 436, 141444.

[30] M. Liu, L. J. Kong, X. M. Wang, J. He, J. J. Zhang, J. Zhu and X. H. Bu, Deciphering of advantageous electrocatalytic water oxidation behavior of metal-organic framework in alkaline media, *Nano Res.*, 2021, 14, 4680-4688.

[31] W. X. Chen, X. W. Zhu, W. Wei, H. R. Chen, T. H. Dong, R. Wang, M. Liu, K. Ostrikov, P. Peng and S. Zang, Neighboring Platinum Atomic Sites Activate Platinum-Cobalt Nanoclusters as High-Performance ORR/OER/HER Electrocatalysts, *Small*, 2023, 19(47), 2304294.

[32] C. Zhang, W. Xu, S. T. Xu, X. Z. Wang, Z. Y. Guan, M. L. Zhang, J. Wu, X. X. Ma, M. L. Wu and Y. F. Qi, Core-shell heterojunction engineering of $Ni_{0.85}Se$-O/CN electrocatalyst for efficient OER, *Chem. Eng. J.*, 2023, 454, 140291.